A Novel fuel electrode enabling direct CO$_2$ electrolysis with excellent and stable cell performance

Yihang Li[a], Bobing Hu[a], Changrong Xia[a]*, Wayne Q. Xu[b], John P. Lemmon[b], Fanglin Chen[c]

[a] Key Laboratory of Materials for Energy Conversion, Chinese Academy of Sciences, Department of Materials Science and Engineering & Collaborative Innovation Center of Suzhou Nano Science and Technology, University of Science and Technology of China, No. 96 Jinzhai Road, Hefei, Anhui Province, 230026, P. R. China.

*Tel: +86-551-63607475; Fax: +86-551-63601696; E-mail: xiacr@ustc.edu.cn (C. Xia)

[b] National Institute of Clean and-Low-Carbon Energy (NICE), Beijing 102211, P. R. China.

[c] Department of Mechanical Engineering, University of South Carolina, 300 Main Street, Columbia, SC 29208, USA.

The theory of distribution of relaxation time

When a lot of sub-processes contribute to the overall impedance, it is often a fraught task to use equivalent circuit models for the evaluation of EIS (electrochemical impedance spectroscopy) data. Therefore, we use a pre-identification method based on the distribution function of relaxation times, named DRT function $g(\tau)$, which can separate polarization processes with different time constants directly from EIS data. A sub-process is described by an equivalent circuit, a parallel connection of a resistance R and a capacitance C. For each equivalent circuit, the time constant is $\tau_i = 1/R_iC_i = 1/2\pi f_i$. Therefore, the cell resistance can be expressed by

$$Z_{pol}(\omega) = \int_0^\infty \frac{g(\tau)}{1+j\omega\tau}d\tau \quad (1)$$

where $\dfrac{g(\tau)}{1+j\omega\tau}$ represents the fraction of the overall polarization resistance with relaxation times between τ and τ+dτ. The mathematical problem with this approach arises from the inversion of Eq. 1, which is necessary in order to extract $g(\tau)$ from the measured EIS data. In this work, we use a Matlab package for regularization.

Electrochemical relaxation characterization

The electrical conductivity relaxation (ECR) technique was performed to determine the surface exchange coefficient (k_{ex}), which is based on the relationship between the electrical conductivity. The change in conductivity, which reflects the change in the oxygen concentration of the sample, after a step-wise change in the ambient oxygen partial pressure (pO_2) is recorded as a function of time. The obtained data are fitted to the appropriate solution of Fick's second law, assuming linear kinetics for the surface exchange reaction, and a linear relationship between the sample conductivity and the oxygen ion concentration within the applied pO_2 step change. The corresponding analytical solution is given by

$$g(t) = \frac{\sigma(t)-\sigma(0)}{\sigma(\infty)-\sigma(0)} = \frac{c(t)-c(0)}{c(\infty)-c(0)} = 1 - \sum_{m=1}^{\infty}\sum_{n=1}^{\infty}\sum_{p=1}^{\infty} \frac{2L_\phi^2 \exp\left(-\beta_m^2 Dt/x^2\right)}{\beta_m^2\left(\beta_m^2 + L_\beta^2 + L_\beta\right)} \times \frac{2L_\gamma^2 \exp\left(-\gamma_n^2 Dt/y^2\right)}{\gamma_n^2\left(\gamma_n^2 + L_\gamma^2 + L_\gamma\right)} \times \frac{2L_\phi^2 \exp\left(-\phi_p^2 Dt/z^2\right)}{\phi_p^2\left(\phi_p^2 + L_\phi^2 + L_\phi\right)} \quad (2)$$

where $g(t)$ is the normalized conductivity, $\sigma(\infty)$ and $\sigma(0)$ are the final and initial conductivities, respectively, and $c(\infty)$ and $c(0)$ are the final and initial oxygen concentrations. The parameters x, y and z are the sample dimensions, while β_m, γ_n, ϕ_p and are the the roots of the transcendental equations as defined by

$$L_\beta = \beta_m \tan\beta_m ; \ L_\gamma = \gamma_n \tan\gamma_n ; \ L_\phi = \phi_p \tan\phi_p \quad (3)$$

Meanwhile, the parameters L_β, L_γ and L_ϕ are defined by

$$L_\beta = \frac{x}{L_c}; L_\gamma = \frac{y}{L_c}; L_\phi = \frac{z}{L_c} \quad (4)$$

where
$$L_c = \frac{D}{k} \quad (5)$$

The parameters obtained from fitting are the chemical surface exchange coefficient, k (m s^{-1}) and the chemical diffusion coefficient, D (m^2 s^{-1}). When the sample is thin enough, which often means its thickness is smaller than the characteristic thickness L_c, the diffusion step is so fast that the incorporation reaction is limited only by the surface step. In addition，the relative

change of the oxygen concentration as a function of time is

$$\frac{\partial c(t)}{\partial t} = -\frac{Sk}{t}\left[c(t) - c(0)\right] \quad (6)$$

Therefore, the experimental data is fitted with the surface exchange controlling E exponential function

$$g(t) = 1 - \exp\left(-\frac{S}{V}kt\right) \quad (7)$$

where S (m²) is the surface area exposed to the gas phase and V (m³) is the sample volume.

The theory of the average metal-oxygen bonding energy

The average metal-oxygen energy (<ABE>) within the perovskite lattice is calculated from the average A-O (<A-O>) and B-O (<B-O>) bond energy. The <ABE> for $A_wB_{1-y-z}B'_yB''_zO_{3-\delta}$ perovskite can be given by:[1]

$$< ABE > = <\text{A-O}> + <\text{B-O}> \qquad (8)$$

$$<\text{A-O}> = \frac{1}{N_A \cdot m} \times (\Delta H_{AmOn} - m \times \Delta H_A - \frac{n}{2} \times D_{O_2}) \qquad (9a)$$

$$<\text{A-O}> = \frac{w}{N_A \cdot m} \times (\Delta H_{AmOn} - m \times \Delta H_A - \frac{n}{2} \times D_{O_2}) \text{ in the case of A-site deficiency} \qquad (9b)$$

$$<\text{B-O}> = \Delta<\text{B-O}> + \Delta<\text{B'-O}> + \Delta<\text{B''-O}> \qquad (10)$$

$$\Delta<\text{B-O}> = \frac{x_B}{N_B \cdot m} \times (\Delta H_{BmOn} - m \times \Delta H_B - \frac{n}{2} \times D_{O_2}) \qquad (11)$$

where w is the molar fraction of A-site cations in A-site deficient compositions; x_B (1-y-z, y, and z) is the molar fraction of B metals; $\Delta H_{A(B)m}$ On and $\Delta H_{A(B)}$ are the enthalpy of formation of one mole of A(B)m On oxides and the sublimation energy of A(B) metal and D_{O2} is the dissociation energy of O_2 (500.2 kJ/mol) at 25 °C. $N_{A(B)}$ is the coordination number of cations on the A and B sites (N_A=12, N_B=6).

For SFM, ΔH_{SrO}=-548 kJ/mol, ΔH_{Fe2O3}=-823 kJ/mol, ΔH_{MoO3}=-1090 kJ/mol, ΔH_{Sr}=164.4 kJ/mol, ΔH_{Fe}=416.4 kJ/mol, ΔH_{Mo}=658.1 kJ/mol. All the thermodynamic data can be obtained from HSC software 5.0.
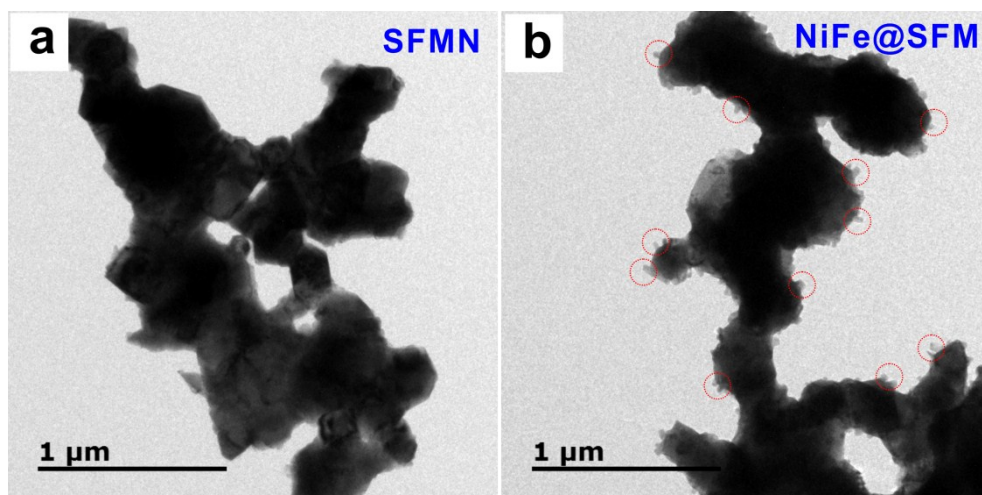
Figure S1 The TEM images of (a) SFMN powders, and (b) NiFe@SFM (SFMN powders reduced in H_2 at 800℃ for 5 h)
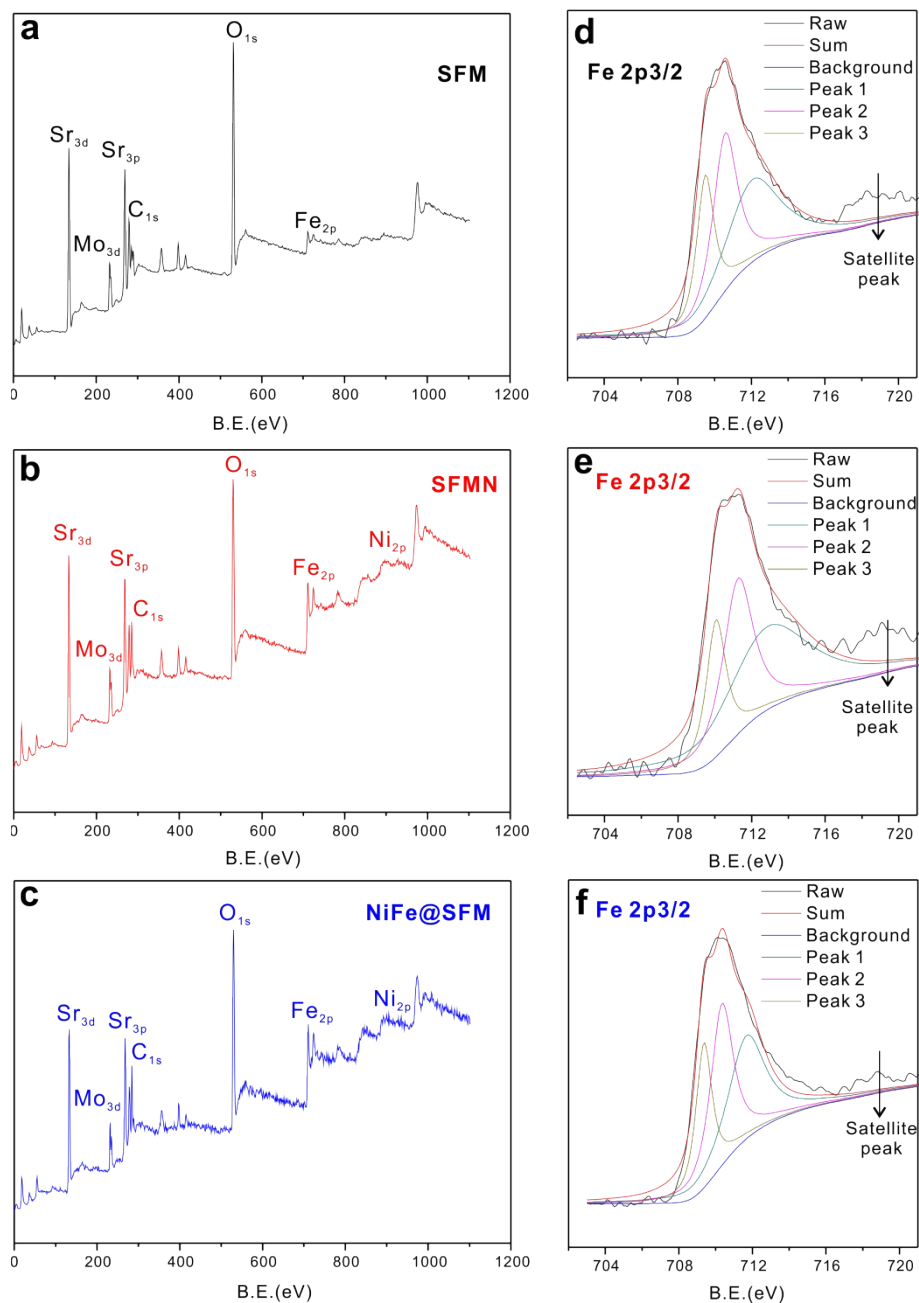
Figure S2 XPS spectra of the survey (a, b and c) and Fe $2p_{3/2}$ fitting profiles (d, e and f) for the

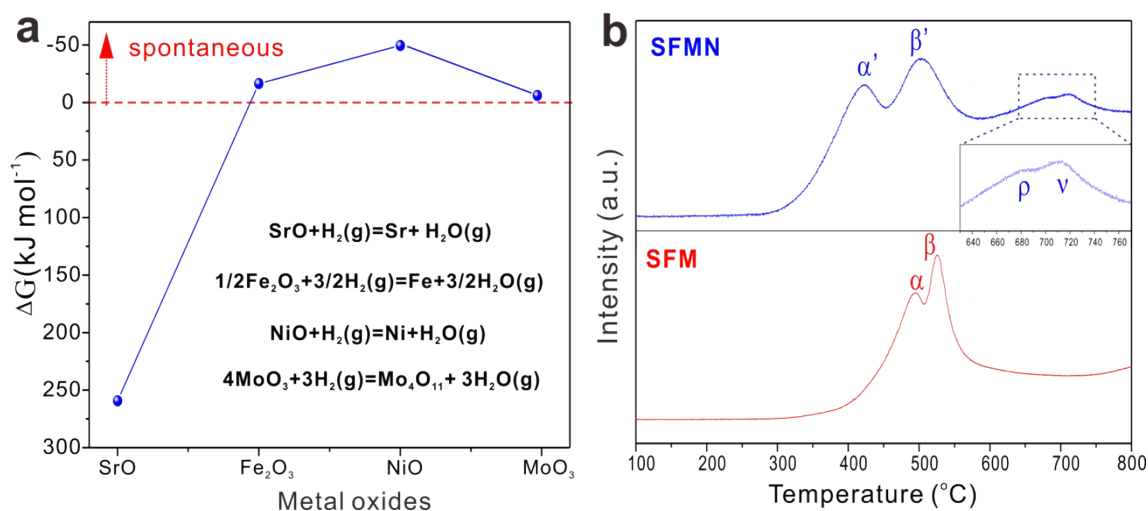SFM, SFMN and NiFe@SFM powders, respectively

Figure S3 (a) Gibbs free energy for the reduction reactions of oxides; (b) TPR profiles in hydrogen for SFM and SFMN powders

Fig.S3a summarizes the Gibbs free energy for the reduction reaction at 800 °C using the thermodynamic data from HSC Chemistry program 5.0. Both Ni and Fe oxides are thermodynamically favorable to be reduced but Ni oxides are easier than Fe oxides. The hydrogen temperature programmed reduction (H_2-TPR) was performed to investigate the reducibility of SFM and NiFe@SFM powder, Fig. S3b. For SFM, in accordance with previous studies, the reduction of Fe^{n+} in SFM perovskite likely occurs through two main steps, i.e., the peak of α at 494 °C and β at 526 °C, corresponding to the reduction of Fe^{4+} into Fe^{3+} and Fe^{3+} into Fe^{2+}. For SFMN, the first reduction peak α' reduced to 422 °C, and the second reduction peak β' to 503 °C. Two additional overlapped peaks appeared at 680 °C and 712 °C, which should be ascribed to the reduction of Ni^{2+} into metallic Ni^0 and Fe^{2+} into Fe^0. With the introduction of A-site deficiency in the SFM perovskite lattice, the reducibility of Fe as well as Ni was remarkably facilitated.
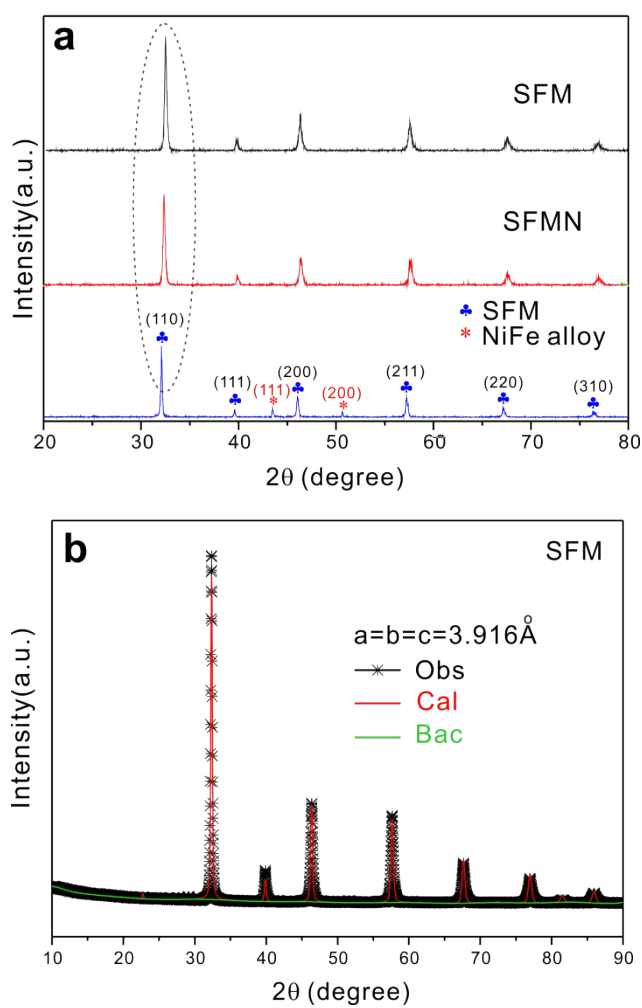
8

Figure S4 (a) XRD patterns for SFM, SFMN and NiFe@SFM powders; (b) Refined XRD profiles of SFM powders. Observed (black), calculated (red), and background (green) for each sample are presented.
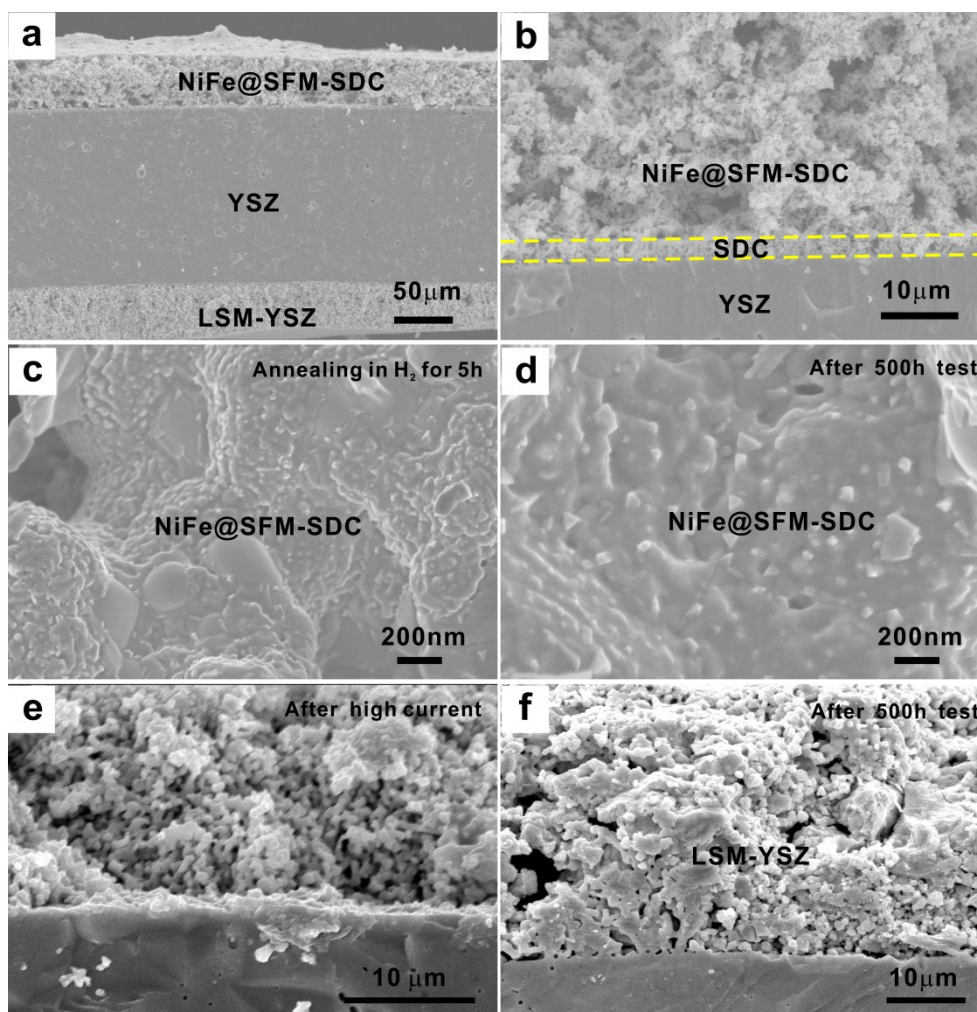
Figure S5 The SEM images: (a) Cross-sectional view of a whole cell consisting of a LSM-YSZ air electrode, a YSZ dense electrolyte, a SDC interlayer and (b) a NiFe@SFM-SDC fuel electrode; (c) a fresh NiFe@SFM-SDC fuel electrode and (d) a post-test NiFe@SFM-SDC fuel electrode; LSM-YSZ oxygen electrodes (e) after 10 hrs test at high current density of 2 A cm^{-2} and (f) after 500 hrs long-term test at 1.3 V.

There are no observable internal cracks, either between fuel electrode and barrier layer or barrier layer and electrolyte (Fig. S5b), indicating that the relatively dense SDC layer has good contact with the fuel electrode and the electrolyte layer. The SDC interlayer will prevent the reaction between the fuel electrode and YSZ electrolyte during the cell fabrication and electrochemical performance testing.
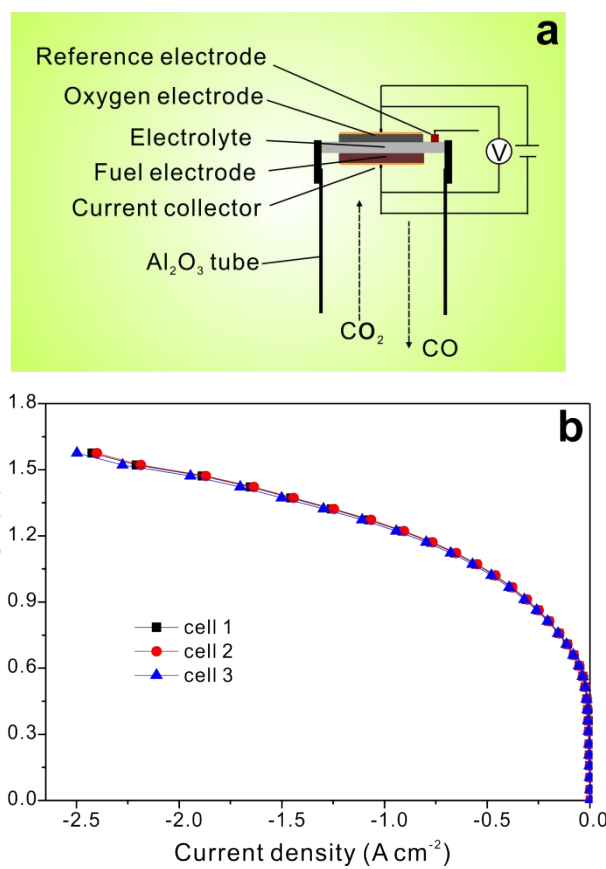
Figure S6 (a) Cell configuration for CO_2 electrolysis operation in present work; (b) IV curves of three cells with NiFe@SFM fuel electrodes at 800°C, indicative of the reproducibility of the results.

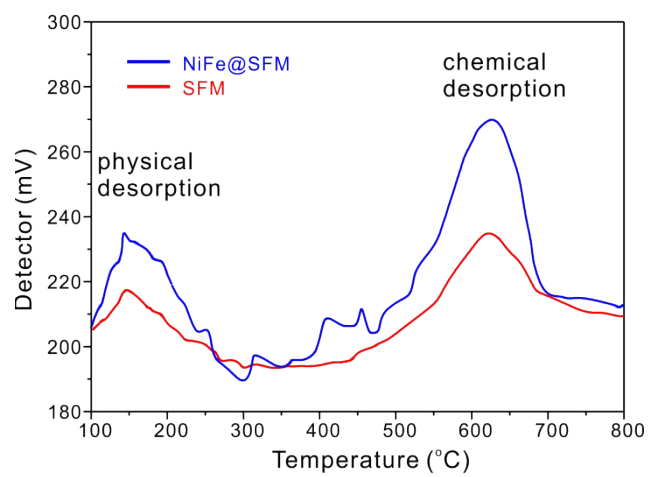**Figure S7** CO_2 TPD profiles for the SFM and NiFe@SFM powders
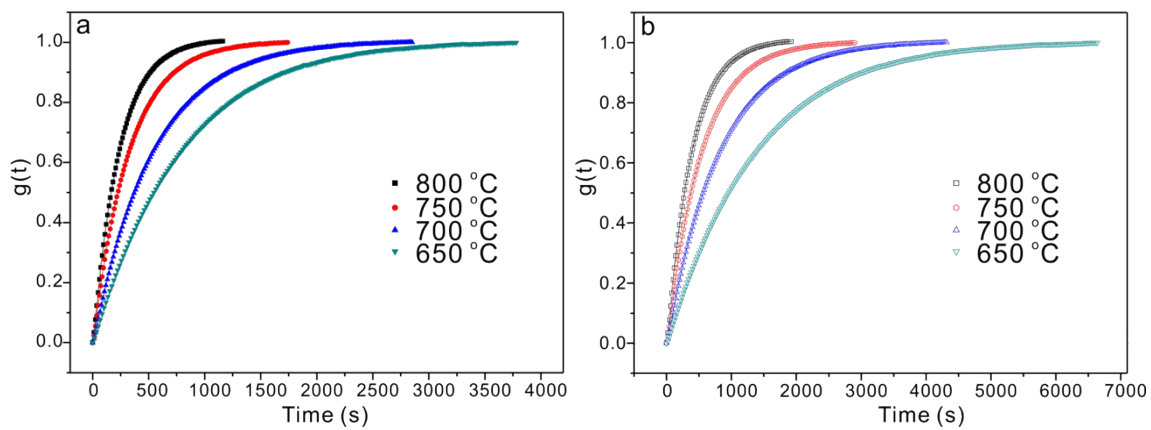
Figure S8 Electrical conductivity relaxation curves of (a) NiFe@SFM and (b) SFM at 650-800

°C after sudden change of oxygen partial pressure.
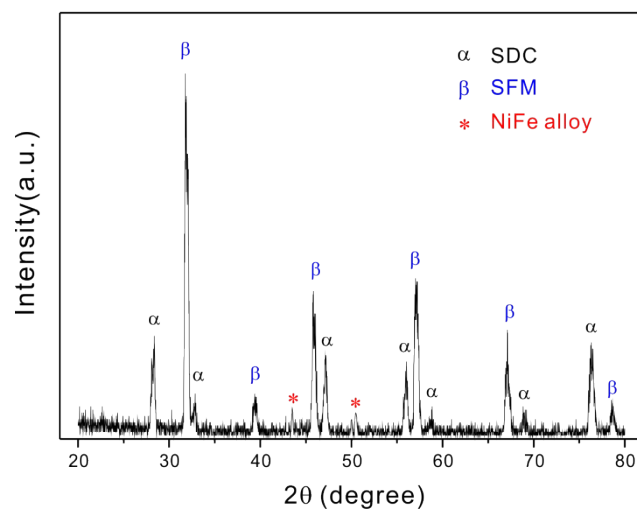
Figure S9 XRD pattern of the NiFe@SFM-SDC fuel electrode after long-term stability test of

500 h for CO_2 electrolysis at 800 ^{o}C
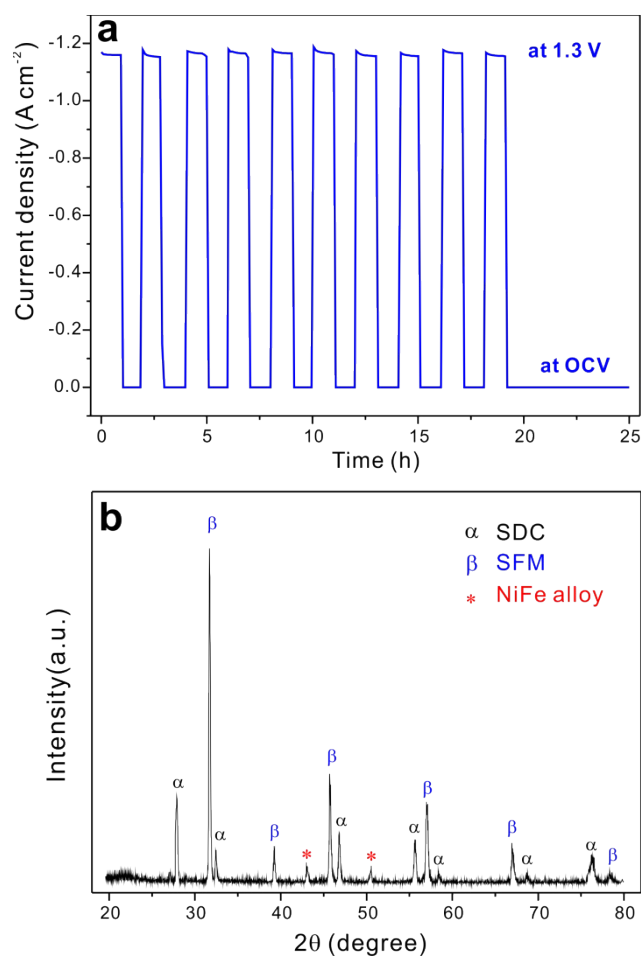
Figure S10 (a) Current density as a function of time of cyclic test under CO_2 electrolysis mode at 1.3 V and OCV mode with interval of 2 h in each mode for 10 cycles; (b) Corresponding XRD pattern for the NiFe@SFM-SDC fuel electrode after the cyclic test

Table S1 The surface metal atom concentration and fitting data of Fe $2p_{3/2}$ for the SFM, SFMN and NiFe@SFM materials through XPS survey

Sample	Fe $2p_{3/2}$			average state	Surface metal atom concentration			
	+4	+3	+2		Sr	Fe	Mo	Ni
SFM	40.22%	36.18%	23.60%	3.16	51.30% (50%)	37.21% (37.5%)	11.49% (12.5%)	- (0)
SFMN	48.00%	31.50%	20.50%	3.27	49.48% (48.72)	35.92% (38.46)	12.19% (10.26)	2.41% (2.56%)
NiFe@SFM	38.65%	37.41%	23.94%	3.14	44.39%	40.63%	10.01%	4.97%

Note: The values in parentheses represent the correspondingly theoretical value.

Table S2 The summary of the Rietveld refinement results for SFM, SFMN and NiFe@SFM materials

Sample	Space group	a (Å)	b (Å)	c (Å)	ωR_p (%)	R_p (%)	χ^2
SFM	$Pm\bar{3}m$	3.916	3.916	3.916	4.43	5.98	2.267
SFMN	$Pm\bar{3}m$	3.920	3.920	3.920	4.92	6.30	1.416
NiFe@SFM	$Pm\bar{3}m$	3.932	3.932	3.932	7.86	6.11	1.975

Table S3 Cell performance at 800 °C for direct CO_2 electrolysis using metal nanocatalysts modified perovskite fuel electrodes through *in-situ* reduction

Initial fuel electrode composition	Nanocatalysts	YSZ electrolyte (mm)	Polarization resistance (Ω cm^2)	Current density at 1.5 V (A cm^{-2})
$(La_{0.75}Sr_{0.25})_{0.9}(Cr_{0.5}Mn_{0.5})_{0.9}Cu_{0.1}O_{3-\delta}$	Cu	2	1.8 (at 1.2V)	0.25 [2]
$(La_{0.2}Sr_{0.8})_{0.9}(Ti_{0.9}Mn_{0.1})_{0.9}Ni_{0.1}O_{3-\delta}$	Ni	1	1.2 (at 1.6V)	0.1 [3]
$(La_{0.2}Sr_{0.8})_{0.95}Ti_{0.85}Mn_{0.1}Ni_{0.05}O_{3-\delta}$	Ni	0.5	0.51 (at 1.6V)	0.43 [4]
$(La_{0.75}Sr_{0.25})_{0.9}(Cr_{0.5}Mn_{0.5})_{0.9}Ni_{0.1}O_{3-\delta}$	Ni	1	1.3 (at 1.2V)	0.2 [5]

Table S4 Cell performance at 800 °C for direct CO_2 electrolysis with different fuel electrode

Fuel electrode	Electrolyte Thickness (mm)	Feeding gas	Temperature (°C)	Polarization resistance (Ω cm^2)	Current density (A cm^{-2})
LST-SDC	YSZ (2)	CO_2	700	16 at 1.3 V	0.05 at 1.5 V [6]
LSTM-SDC	YSZ (2)	CO_2	800	2.1 at 1.6 V	0.12 at 1.5 V [7]
LSCM-SDC	YSZ (2)	CO_2	800	2.7 at 1.5 V	0.09 at 1.5 V [8]
Ce-LSCrFe-YSZ	YSZ (0.3)	CO_2	850	0.211 at 1.2 V	0.8 at 1.5 V [9]
Ag-GDC	YSZ(2)	CO_2	800	0.9 at 0.99 V	0.75 at 1.5 V [10]
Ni-Fe (9:1)	LSGM (0.3)	CO_2/CO (50:1)	800	4.03 at Voc	0.87 at 1.5V [11, 12]
Ni-Fe-LSFM	LSGM (0.3)	CO_2/CO (50:1)	800	2.32 at Voc	1.50 at 1.5 V [12]
SFM-YSZ	YSZ (0.01)	CO_2	800	0.41 at Voc	1.10 at 1.5 V [13]

Notes: LST=$La_{0.2}Sr_{0.8}TiO_{3+\delta}$, LSTM = $La_{0.2}Sr_{0.8}Ti_{0.5}Mn_{0.5}O_{3-\delta}$,

LSCM= $La_{0.75}Sr_{0.25}Cr_{0.5}Mn_{0.5}O_{3-\delta}$, Ce-LSCrFe=$La_{0.65}Sr_{0.3}Ce_{0.05}Cr_{0.5}Fe_{0.5}O_{3-\delta}$,

LSGM= $La_{0.9}Sr_{0.1}Ga_{0.8}Mg_{0.2}O_{3-\delta}$, LSFM= $La_{0.6}Sr_{0.4}Fe_{0.8}Mn_{0.2}O_{3-\delta}$, SFM=$Sr_2Fe_{1.5}Mo_{0.5}O_{6-\delta}$

Table S5 The fitting results of the EIS for two different types of cells obtained from 800°C

Temperature (°C)	Fuel electrodes	Rs (Ω cm^2)	R$_1$ (Ω cm^2)	R$_2$ (Ω cm^2)	R$_3$ (Ω cm^2)
800	NiFe@SFM-SDC	0.5624	0.0502	0.1207	0.0934
	SFM-SDC	0.5666	0.0523	0.1473	0.1425

Table S6 The changes of the oxygen partial pressure at 650-800 °C for ECR measurement

Temperature (°C)	CO:CO$_2$ (2:1) (atm)	CO:CO$_2$ (1:1) (atm)
800	9.49×10^{-20}	3.79×10^{-19}
750	4.30×10^{-21}	1.72×10^{-20}
700	1.42×10^{-22}	5.66×10^{-22}
650	3.21×10^{-24}	1.28×10^{-23}

References

[1] R.L. Cook, A.F. Sammells, Solid State Ionics, 45 (1991) 311-321.

[2] H.X. Li, G.H. Sun, K. Xie, W.T. Qi, Q.Q. Qin, H.S. Wei, S.G. Chen, Y. Wang, Y. Zhang, Y.C. Wu, Int J Hydrogen Energ, 39 (2014) 20888-20897.

[3] Y. Li, K. Xie, S. Chen, H. Li, Y. Zhang, Y. Wu, Electrochim Acta, 153 (2015) 325-333.

[4] L. Ye, M. Zhang, P. Huang, G. Guo, M. Hong, C. Li, J.T. Irvine, K. Xie, Nat Commun, 8 (2017) 14785.

[5] C. Ruan, K. Xie, Catal Sci Technol, 5 (2015) 1929-1940.

[6] Y.X. Li, J.E. Zhou, D.H. Dong, Y. Wang, J.Z. Jiang, H.F. Xiang, K. Xie, Phys Chem Chem Phys, 14 (2012) 15547-15553.

[7] W.T. Qi, Y. Gan, D. Yin, Z.Y. Li, G.J. Wu, K. Xie, Y.C. Wu, J Mater Chem A, 2 (2014) 6904-6915.

[8] S.S. Xu, S.S. Li, W.T. Yao, D.H. Dong, K. Xie, J Power Sources, 230 (2013) 115-121.

[9] Y.-Q. Zhang, J.-H. Li, Y.-F. Sun, B. Hua, J.-L. Luo, Acs Appl Mater Inter, 8 (2016) 6457-6463.

[10] Y.M. Xie, J. Xiao, D.D. Liu, J. Liu, C.H. Yang, J Electrochem Soc, 162 (2015) F397-F402.

[11] S.J. Wang, A. Inoishi, J. Hong, Y. Ju, H. Hagiwara, S. Ida, T. Ishihara, J Mater Chem A, 1 (2013) 12455-12461.

[12] S.J. Wang, H. Tsuruta, M. Asanuma, T. Ishihara, Advanced Energy Materials, 5 (2015).

[13] Y. Li, P. Li, B. Hu, C. Xia, J. Mater. Chem. A, 4 (2016) 9236-9243.